Stability Analysis of Hypervelocity Ballistic-Range Data

A. Hameed*, J. H. Chen[†], and N. J. Parziale[‡]
Stevens Institute of Technology, Hoboken, NJ, 07030, USA

S. Dungan[§], B. Saikia[¶], and C. Brehm[‖]
University of Maryland, College Park, MD, 20740, USA

This paper analyzes hypervelocity ballistic-range transition experiments performed by Sheetz using the STABL and CHAMPS stability techniques. Comparison between the two computational techniques is performed for two experiments and the stability calculations are found to be nominally consistent. In the experiments where the second mode should dominate transition, the N-factor of transition was found to be higher than that in a conventional hypersonic facility. An assessment was conducted of the spread of the N-factor at the transition location for a subset of experiments where the geometry and physics governing transition should be the same. Conventional transition location correlations are presented and, although they are not mechanism based, the correlations do appear to separate the data into distinct groupings which can inform further mechanism-based analysis.

I. Introduction

The instability and transition problem is influenced by the noise environment via boundary-layer receptivity [1–5]. High-speed boundary-layer transition has been studied in ground test extensively and the effect of tunnel noise on transition data has been reviewed by Schneider [6, 7]. Influential disturbances can include acoustic waves, entropy inhomogeneity, and vortical perturbations, in addition to micro and macro scale particulates [8]. Researchers believe that the primary source of noise in a ground-test facility is the turbulent boundary layer on the nozzle wall [6–9]. This led to multi-decade efforts to develop hypersonic wind tunnels with low disturbance levels [10–12].

One way to circumvent the issue of noise radiating from turbulent boundary layers on high-speed wind tunnel walls is to use a hypervelocity ballistic-range and launch a test article through an environmental chamber and observe the transition location. In the 1960s and 1970s, this was the strategy of Lyons and Sheetz [13–17], Potter[18–21] and Reda [22–24]. More recent work on this topic was conducted by Swanson and Daniel [25] and Mueschke et al. [26].

This paper analyzes hypervelocity ballistic-range transition experiments performed by Lyons and Sheetz [13, 14], which are further described in Sheetz [15, 16, 17]. Stability analysis for these experiments was performed using the STABL [27, 28] software suite to determine what the so-called "N-factor" of transition is for hypervelocity ballistic-range transition experiments. The linear-stability computations are compared with wavepacket tracking simulations and time-spectral solution of the disturbance flow field employing the CHAMPS solver. A discussion is presented of the results, including a comparison between the computational approaches, an assessment of the spread of N-factor at the transition location, and a presentation of conventionally used transition location correlations.

II. Experiment Conditions of Historical Tests

The tests analyzed in this work were conducted by Sheetz [17] in 1969 at the Naval Ordnance Laboratory (NOL) Pressurized Ballistic Range and the NOL 1000-foot Hyperballistics Range. In these experiments, multiple shadowgraph and schlieren stations were used along the ballistic range to photograph the passing models and estimate the location of boundary-layer transition. The model geometries examined in these ballistic-range tests were: a nominally sharp cone with a 5° half-angle and a varying base diameter, and blunt cones with a 3°, 5°, 6.3°, and 9° half-angle. The

---

*Graduate Student, Mechanical Engineering, 1 Castle Point on Hudson, Hoboken, New Jersey, 07030, USA.

[†]Graduate Student, Mechanical Engineering, 1 Castle Point on Hudson, Hoboken, New Jersey, 07030, USA.

[‡]Associate Professor, Mechanical Engineering, 1 Castle Point on Hudson, Hoboken, New Jersey, 07030, AIAA Associate Fellow.

[§]Graduate Student, Aerospace Engineering, 4298 Campus Drive, College Park, Maryland, 20742, USA.

[¶]Postdoctoral Scholar, Aerospace Engineering, 4298 Campus Drive, College Park, Maryland, 20742, USA.,

[‖]Associate Professor, Aerospace Engineering, 4298 Campus Drive, College Park, Maryland, 20742, USA, Senior AIAA Member.

models were constructed from tool steel or titanium, and an average center-line surface finish of 1 to 6 microinches was reported [17]. The sharp-cone models were launched through the ballistic range at a freestream Mach number varying from Mach 3 to 9, while the blunted models were launched at freestream Mach numbers varying from Mach 6 to 15. To analyze the effect of the wall-temperature ratio, a 21 foot temperature-controlled section was constructed in the NOL Pressurized Ballistic Range[17]. The region was able to be cooled to a reported 89 K and heated to 890 K. Table 1 provides the model geometries and experimental conditions for each shot examined in this paper. The mean flow around the models was calculated using the data-parallel lower-upper relaxation (DPLR) method as described by Wright et al. [29], Johnson [28], and Johnson et al. [27]. The freestream and boundary-layer edge properties at the transition location shown in Table 1 were extracted from the mean-flow solutions during the post-processing of the CFD results.

III. Stability Analysis using STABL

The STABL software suite was one of the techniques used to perform stability analysis for the experiments completed by Sheetz. In STABL, the method of normal modes is first applied to the reacting Navier-Stokes equations, where it is assumed that the boundary layer is quasi-parallel, the gas is in thermo-chemical non-equilibrium, and the disturbances have the form

$$q'(s, z, t) = \hat{q}(y) \exp(i(\alpha s + \beta z - \omega t)), \tag{1}$$

where q' is a disturbance at a position along the generator of the cone s, azimuthal position z, and time t. The amplitude of the disturbance is considered to be only a function of the wall-normal distance, $\hat{q} = \hat{q}(y)$. The stream-wise wave number is α, the azimuthal wave number is β, and the angular frequency is ω. The spatial linear-stability problem is analyzed where the frequency (ω) is real and the wave numbers are complex ($\alpha = \alpha_r + \alpha_i$); non-zero azimuthal wavenumbers (β) are not considered in this analysis, as disturbance is assumed to be two-dimensional. The linear-stability calculation results are then used as initial values for the parabolized stability equation (PSE) analysis, which is used to account for the non-parallel nature of the boundary layer. This is done with a parabolized stability equation solver called PSE-Chem which computes linear-stability diagrams and amplification curves. The amplification factor, N, is computed as

$$N = \int \sigma \, ds, \tag{2a}$$

$$\sigma = -Im(\alpha) + \frac{1}{2E}\frac{dE}{ds}, \tag{2b}$$

$$E = \int_\Omega \overline{\rho}\left(|\hat{u}|^2 + |\hat{v}|^2 + |\hat{w}|^2\right) dV, \tag{2c}$$

where σ is the growth rate, α is the wavenumber along a generator of the cone, and E is the disturbance kinetic energy. The software allows for the simulation of finite-rate chemistry effects and transition-vibrational energy exchange to predict the growth rate of naturally-occurring disturbances in hypersonic flows [30]. In this paper, the stability analysis performed using STABL assumed the second-mode instability to be the dominant transition mechanism.

A. Grid Generation and Mean-Flow Analysis

The grid-generation module of the STABL software suite was used to generate grids for each experiment analyzed in this paper. All the grids used in the simulations were set to approximately 0.2 m long, regardless of the length of the model used for the specific experiment. Fig. 1 shows a grid used for shot 5474, and is representative of the grids used for models with a nominally sharp nose tip.
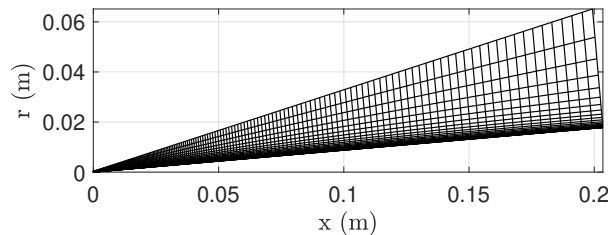

Fig. 1   Grid used for the mean-flow analysis of shot 5474, which featured a sharp cone model.

For the analysis of models with blunt nose tips, the grid tailoring routine was employed within STABL's software suite to capture a shock-fitted grid. Fig. 2 depicts the grid tailoring process for shot 5697. Fig. 2a shows the initial grid used to perform the initial mean-flow solution. This grid is intentionally oversized to ensure the shock is completely captured. Using this initial grid, the mean flow is resolved with particular attention paid to the blunt nose tip to ensure the local residual in this region is approximately 1e-12. After resolving the flow around the cone's nose tip, we then freeze the solution around this area and continue to resolve the solution along the rest of the model. A different set of CFL values are used for this iteration of the CFD solution. The mean flow is deemed resolved once the residual throughout the cone is observed to reach approximately 1e-12.
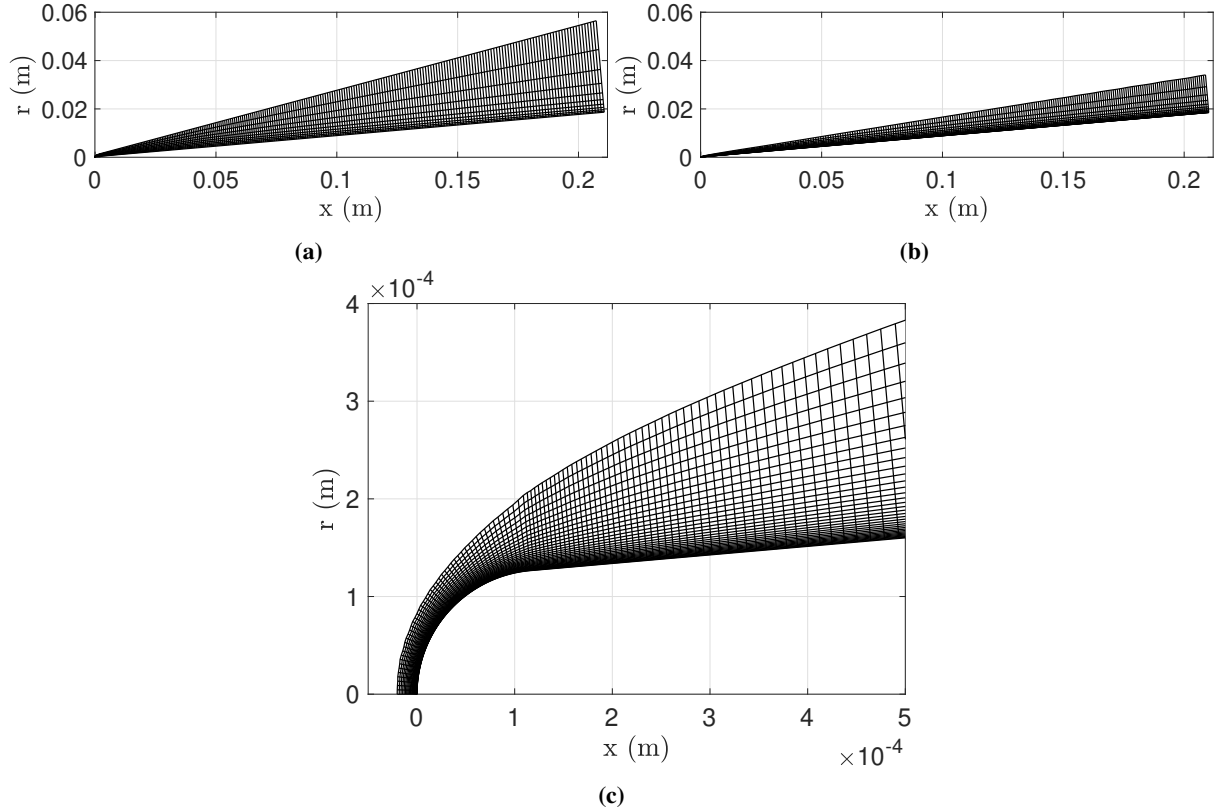

(a)

(b)

(c)

Fig. 2 Modification of the grid used for the mean-flow analysis of shot 5697, which featured a blunt cone. (a) The original grid used to perform an initial mean-flow simulation. (b) Grid generated by STABL's grid tailoring routine. (c) A close-up view of the tailored grid at the blunt nose tip of the cone.

Next, using the grid-tailoring routine in STABL's flow analysis module, we post-process the resolved mean-flow solution obtained using the initial grid. As shown in Fig. 2b, STABL adjusts the upper grid definition and body-normal spacing to better fit the grid to the shock. Fig. 2c shows the tailored grid around the model's blunted nose tip. In a process similar to the one used with the initial grid, the mean-flow analysis is rerun with the tailored grid to produce a higher-quality mean-flow solution to input into the stability analysis. The mean-flow analyses for all shots were performed on a high-performance computing cluster. Adjustments were made to the grid, the maximum number of iterative steps, and the CFL ramp to achieve residual values of approximately 1e-12. Results of the mean-flow simulation performed on the tailored grid for shot 5697 are presented in Fig. 3 and are representative of results for the other experiments with sharp and blunt cones. As shown in Fig. 3a, the residual is approximately 0 along the cone, with a slight increase towards the trailing edge. We chose not to resolve the mean flow further as the increase in the residual occurred far away from the observed transition locations by Sheetz. Fig. 3b shows contours of Mach number at the blunt nose tip. As seen in the figure, the shock is adequately captured by the tailored grid. Fig. 3c shows that y^+_{wall} value is less than unity along the length of the cone, which suggests enough points within the boundary layer.
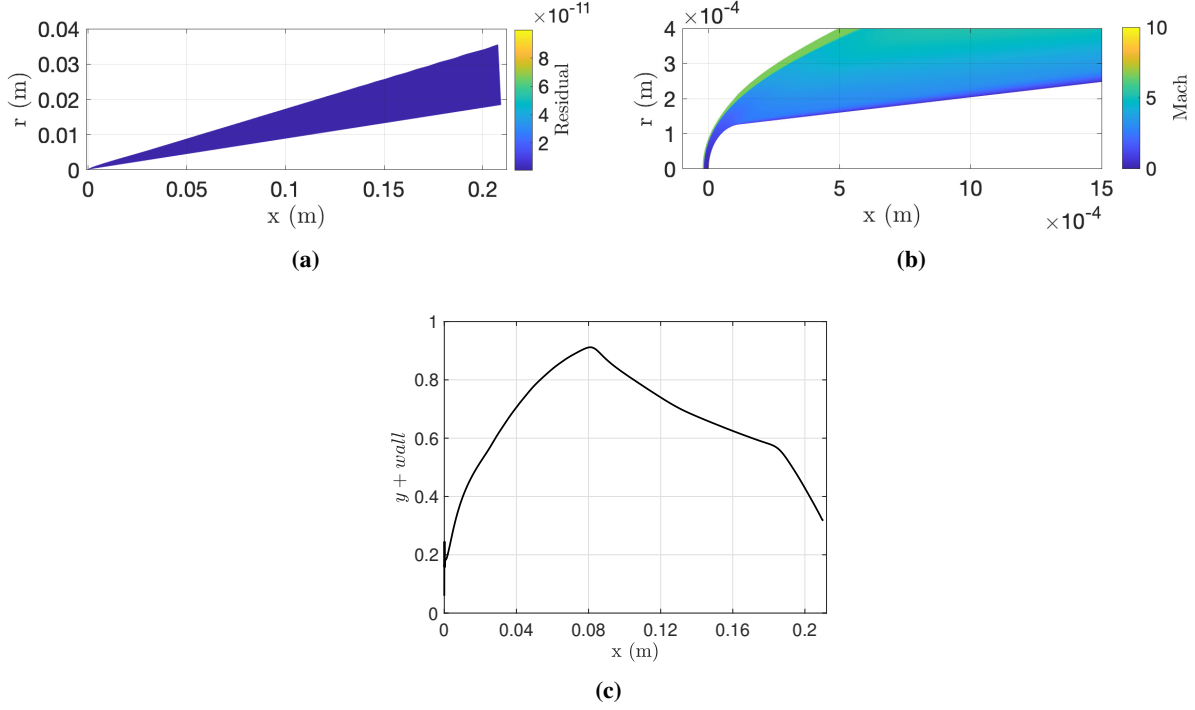
3

(a)

(b)

(c)

Fig. 3   Mean-flow simulation results for shot 5697. (a) The residual is 1e-12 throughout the cone. (b) The Mach profile at the leading edge shows that the shock is adequately captured with the tailored grid. (c) The y^+_{wall} wall parameter remains below unity throughout the length of the model, suggesting the local grid quality is sufficient.

B. Stability Analysis

The stability analysis of the flow is done through the parabolized stability equation solver within STABL, PSE-Chem. Due to the extreme flow conditions experienced during these shots, and the anticipation of higher amplification rates, we increased the maximum amplification rates considered allowable by STABL from the default value of ±200. The initial stability analysis performed for many of the shots suggested an increase in resolution was necessary to reduce the striations seen at the leading edge of the model in the stability diagrams. As a result, each stability analysis typically took 12-36 hours on a high-performance computing cluster depending on the number of nodes available and the resolution of the grid used in the stability analysis.

IV. Stability Analysis using CHAMPS

Stability analyses were also performed using the Cartesian, Higher-Order, Adaptive, Multi-Physics Solver (CHAMPS). Specifically, the nonlinear disturbance equations (NLDE) were first solved using adaptive mesh refinement (AMR). A pulse disturbance is introduced downstream of the blunted nose and the code evolves the resulting flow field in time. The AMR tracks the most important flow quantities of interest, here the second mode dominated wavepacket, as they grow or decay downstream. The simulation approach has been referred to as adaptive mesh refinement wavepacket tracking (AMR-WPT) or sometimes also as disturbance flow tracking (AMR-DFT). More details of the AMR-WPT solver and a large number of validation cases can be found in Refs. 31–33. The unsteady wall pressure distribution in space and time is decomposed using fast Fourier transforms revealing which disturbance frequencies will be amplified. The number of points required for such a simulation as a function of timestep (iteration) is shown in figure 4a. It is important to note that this NLDE simulation (equivalent to a direct numerical simulation) only requires, at most, 100,000 grid points and can be run in a few hours for a broad range of frequencies. A snapshot of the AMR mesh and the flow field it is tracking is shown in figure 4b. The black lines enclose the Cartesian mesh blocks where each block is comprised of 24 points in the x and y coordinate directions (right and up in figure 4b, respectively). The pressure contours also shown in figure 4b demonstrate the ability of the refinement strategy to effectively track the second mode dominated disturbance wave
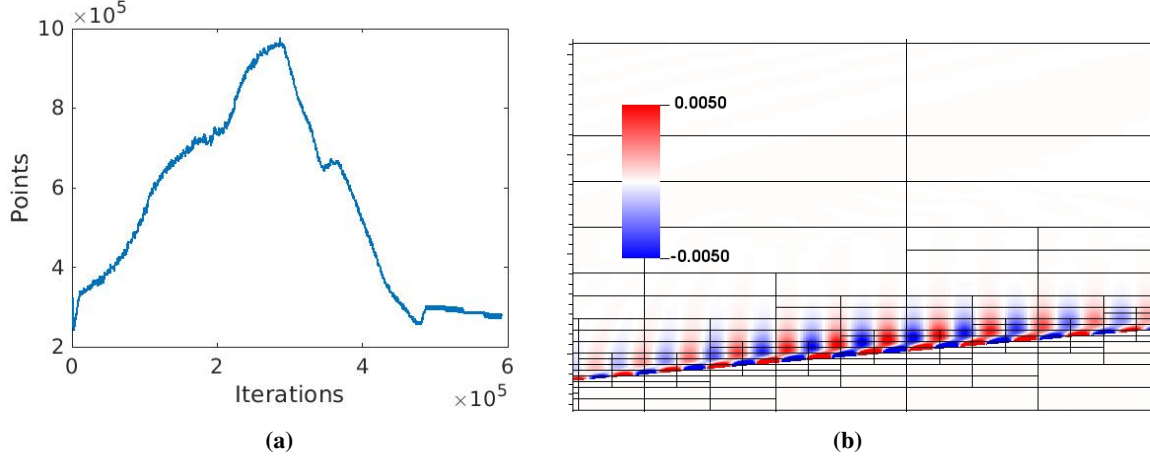
4

Fig. 4 Shot 5697: (a) Time history of the number of grid points used in the 2D AMR wave packet tracking simulation. (b) Cartesian mesh blocks laid on top of the instantaneous pressure contours of the second mode dominated wave packet.

packet as it propagates inside the cone's boundary layer.

To perform receptivity studies and for cross-validation, we used the time-spectral disturbance flow solver [34, 35] which is more efficient for individual frequencies. Since this work aims to conduct a linear receptivity study, two collocations points or time samples are used to solve for the periodic steady-state directly. Instead of using a time-stepping or marching scheme for the time discretization, the temporal derivatives are discretized with the help of a spectral differentiation operator $\mathbf{D}_N$, where N is the number of samples of the solution. By representing the steady state residual $\tilde{\mathbf{R}}$ and the forcing term of the disturbance as $\tilde{\mathbf{S}}$, the solution to the linear disturbance equation can be obtained by a direct inversion of the following system of equations

$$\left(\underline{\tilde{\mathbf{\Gamma}}} \underline{\mathbf{D}_N} - \underline{\mathbf{J}_R} \right) \tilde{\mathbf{Q}} = \tilde{\mathbf{S}}, \tag{3}$$

where $\underline{\tilde{\mathbf{\Gamma}}} = \partial\tilde{\mathbf{U}}/\partial\tilde{\mathbf{Q}}$ is the primitive to conservative variable transformation matrix, $\underline{\mathbf{D}_N}$ is time spectral differentiation matrix, $\tilde{\mathbf{Q}}$ is the primitive variable disturbance flow vector, and $\tilde{\mathbf{S}}$ contains the forcing terms used to introduce disturbances in the flow field. In the above expression, numerical Jacobians, $(\partial\tilde{\mathbf{R}}/\partial\tilde{\mathbf{Q}})_{num}$, are used to approximate the Jacobian matrix, $\underline{\mathbf{J}_R}$, of the right-hand-side residual $\tilde{\mathbf{R}}$. We have made use of the PETSc (Portable, Extensible Toolkit for Scientific Computation) library [36] and linear direct solvers from the external package MUMPS (MUltifrontal Massively Parallel sparse direct Solver) [37] for the direct inversion of Eq. 3 in the limit of infinite local CFL (Courant–Friedrichs–Lewy number). The disturbance is introduced by employing continuous time-periodic volume forcing, which can be expressed as

$$S(x, y, t) = A \ \sin(\frac{2\pi(x - x_s)}{\Delta x_w}) \ \exp(-\frac{(y - y_o)^2}{\sigma_y}) \ \cos(2\pi f t). \tag{4}$$

In the above expression, the width of the forcing slot is Δx_w, which starts at x_s in the streamwise direction. The disturbances are introduced at y_o in the wall-normal direction with a forcing frequency f, and σ_f is the standard deviation of the distribution. To conduct the receptivity study, slow acoustic, fast acoustic, vorticity, and entropy waves are forced at the free stream, either of which will generate all four types of waves downstream of the bow shock. The analytical expressions for these waves are obtained by solving the linearized Euler equations assuming a uniform mean flow. More details about the introduced freestream disturbances can be found in [38–40].
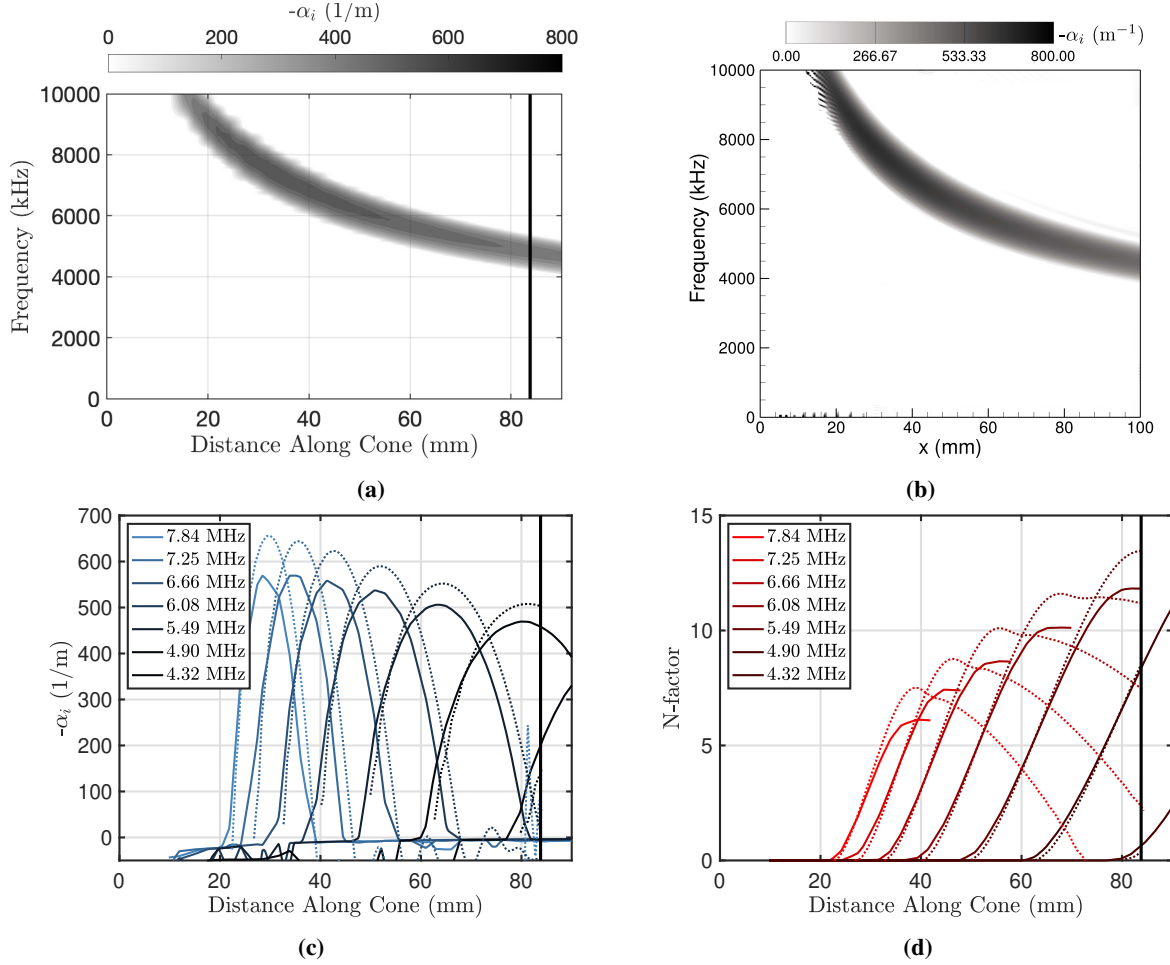
5

Fig. 5   Linear-stability diagrams for shot 5697 as determined by (a) STABL and (b) CHAMPS. (c) Growth rate and (d) N-factor as determined by STABL (solid lines) and CHAMPS (dotted lines) at various frequencies for shot 5697. The vertical black line at approximately 84 mm along the cone represents the observed location of transition.

V. Results

A. Comparison of Stability Analysis Methods

In this section, we present a comparison of the results between the two different stability analysis techniques, STABL and CHAMPS. Fig. 5 shows the stability analysis results for shot 5697, which was an experiment performed using a model with a nose-tip bluntness of R_N = 127 µm. The stability diagrams computed by STABL and CHAMPS are presented in Fig. 5a and Fig. 5b, respectively. We note the very high disturbance frequencies and growth rates for these experiments. The vertical black line in Fig. 5a represents the observed transition location in the experiment, as reported by Sheetz. In Fig. 5c, we present the growth rate at various frequencies along the model as calculated by STABL (solid lines) and CHAMPS (dotted lines). For each frequency plotted, CHAMPS consistently computes a higher growth rate. However, the error between the two computational methods decreases as the frequency is decreased. We suspect this is due to non-equilibrium effects that are accounted for in STABL but not in CHAMPS. Similar observations were made by Johnson et al. [27] for reacting and non-reacting disturbances at similar enthalpies. The N-factors computed by CHAMPS (dotted lines) at these distinct frequencies are also higher than those computed by STABL (solid lines). However, the shape of the N-factor curve prior to each peak matches very well between the two techniques.

A similar comparison between the two stability analysis techniques is made for shot 5708 in Fig. 6. Shot 5708 was an experiment performed using a model with a blunter nose tip (R_N = 305 µm) and a less acute cone half-angle (6.3°).
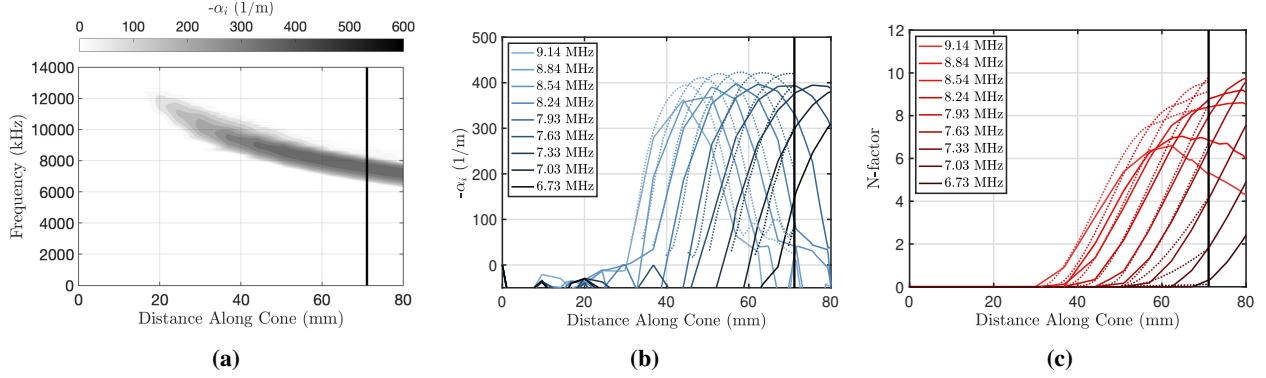
Fig. 6   (a) Linear-stability diagram for shot 5708 as determined by STABL. (b) Growth rate and (c) N-factor as determined by STABL (solid lines) and CHAMPS (dotted lines) at various frequencies for shot 5708. The vertical black line at approximately 71 mm along the cone represents the observed location of transition.

The growth rate curves computed by STABL exhibit discontinuous features, which are a result of the interpolation method used during the post-processing of the data. Regardless, for each frequency plotted, the maximum growth rate as determined by STABL occurs at approximately the same location as computed by CHAMPS. The difference in the predicted growth rate between the two analysis techniques remains, however, the error is lower and decreases moving down the cone. The general shape of the N-factor curve matches the CHAMPS result until it begins to deviate near the location of the maximum N-factor, resulting in a lower computed N-factor by STABL.

B. Assessment of Transition Location Consistency using N-Factor

In this section, we assess the spread of the N-factor at the transition location for cases where the geometry and flow conditions are similar enough that the physics governing transition should be the same. These cases are shots 5036 - 5499 in Table 1 and represent a subset of experiments featuring a sharp, $5°$ half-angle cone at sufficiently high edge Mach number to suggest that the second-mode instability dominates transition. The N-factors at the transition location for these cases are appreciably higher than one would expect in a conventional, noisy hypersonic wind tunnel, $N_T^{2M} > 5$. For these experiments, the lowest N-factor at the observed transition location was $N_T^{2M} = 7.8$ (shot 5469) and the highest N-factor at the observed transition location was $N_T^{2M} = 14.3$ (shot 5039).

An N-factor analysis was performed for each experiment in this subset by comparing the observed transition location with the distance along the cone when the maximum N-factor reached 7.8 and 14.3. Results of this analysis are presented in Fig. 7. As shown in Fig. 7a, there is considerable spread observed for each experiment. For example, for shot 5040, the observed transition location was 0.102 m along the model at a transition N-factor of 12.8. Fig. 7a shows that the calculation for this experiment reached an N-factor of 7.8 at 0.05 m and an N-factor of 14.3 at 0.12 m along the cone. For the 0.12 m model used in this experiment, this represents approximately 60% of the model length.

This spread in transition prediction using the N-factor is also shown by comparing experiments in which the same model geometry was used at nominally the same experimental conditions. In this subset of experiments, shots 5039 and 5040 were performed at unit freestream Reynolds numbers that differed by approximately 7% but the transition N-factor differed by approximately 10%. More drastically, shots 5041 and 5042 featured a 2% difference in the unit freestream Reynolds number but a 22% difference in the transition N-factor. Finally, shots 5467, 5468, and 5470 were performed at nominally the same conditions, however, the N-factor at the transition location differed by approximately 24%.

For each experiment, we next non-dimensionalize the abscissa of Fig. 7a using the edge unit Reynolds number. The result is presented in Fig. 7b. Although the spread between the edge Reynolds number at the transition location and the edge Reynolds number at the locations where $N_T^{2M} = 7.8$ and 14.3 is still present within each shot, the non-dimensionalization appears to collapse the dataset into two distinct groupings dependent on the edge Reynolds number. The shots in black represent experiments with an average $Re_E^{Unit} = 7.7 \times 10^7$ m^{-1} and the shots in blue represent experiments with an average $Re_E^{Unit} = 1.4 \times 10^8$ m^{-1}. The reason for this spread is the subject of ongoing work- preliminary analysis suggests a more careful inspection of the stability calculations for the three outlying cases highlighted in blue is necessary.
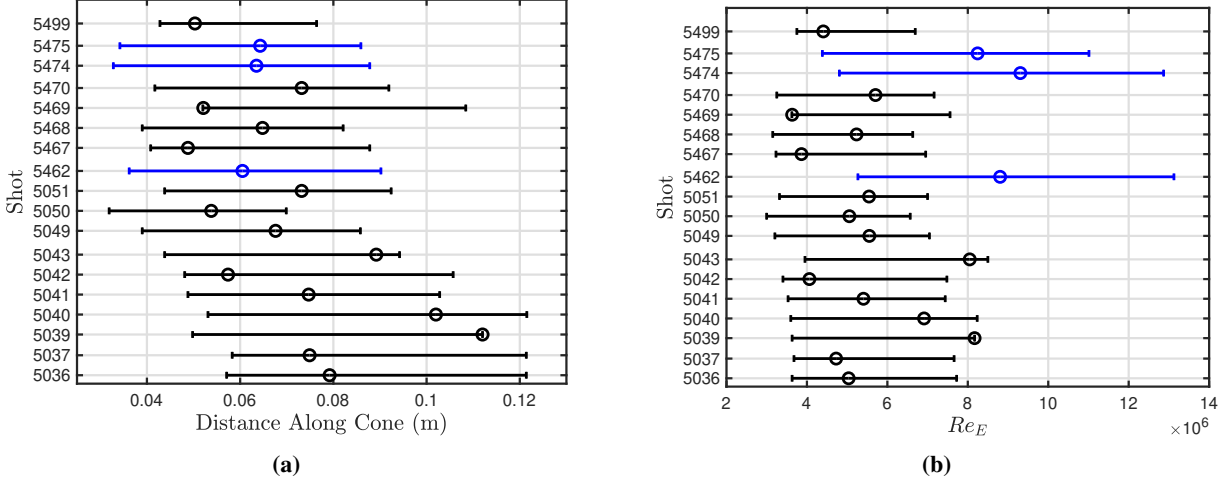
Fig. 7 N-factor analysis for experiments with a 5° half-angle cone and sharp nose tips at high edge Mach number. (a) The observed transition location for the experiments is denoted by the circle marker. For each experiment, the error bars indicate the location along the cone where the maximum N-factor reaches 7.8 (lowest maximum N-factor in this set of experiments) and where the maximum N-factor reaches 14.3 (highest maximum N-factor in this set of experiments). (b) Data from (a) non-dimensionalized using the edge unit Reynolds number at the transition location for each experiment.

C. Traditional Transition Correlations

Correlations between parameters relevant to boundary-layer transition that have been suggested in the literature are presented in this section. For each shot, flow parameters based on the edge conditions at the observed transition location are extracted from the mean-flow solution and the maximum N-factor at the transition location is determined by processing the stability results. The results are presented as filled data points, with the fill color representative of the nose radius of the model for the specific experiment.

In Fig. 8a, we plot the transition parameter, $Re_{\theta,E}/M_E$, where $Re_{\theta,E}$ is the momentum thickness Reynolds number, divided by the edge Mach number at the transition location. We separate the data points into three groupings: A, B, and C. The experiments in group A featured both nominally sharp and slightly blunt models with relatively high edge momentum thickness and transition Reynolds numbers and Mach numbers. Notably, with few outliers, there is a distinct separation between the sharp and blunt experiments within this data set. The shots performed with slightly blunt models remain below a value of $Re_{\theta,E}/M_E \approx 150$ and those performed with sharp models remain above this value of the transition parameter. The experiments in group B featured models with the largest nose bluntness, which subsequently decreased the edge Reynolds number, momentum thickness Reynolds number, and Mach number.

Additional information was ascertained for these groups by plotting the N-factor at the transition location against the edge Mach number at the transition location (Fig. 8b), and the previously defined transition parameter (Fig. 8c). The same groupings used previously are applicable to these figures, however, these groups are more clearly separated. Here, we see that the experiments in group A all feature $N_T^{2M} > 6$ and the edge Mach number at the transition location is greater than 4. This suggests that in these experiments, the hypersonic, second-mode instability was the dominant transition mechanism and this assumption was correctly applied during the stability analysis performed using STABL.

The experiments in group B featured low N-factors and moderate edge Mach numbers. In these experiments, the second-mode instability was not found to be the dominant transition mechanism and alternative paths to transition were analyzed. One of the experiments in group B was shot 5776, which will be analyzed in detail in subsection V.D.

The experiments in group C featured low N-factors and low edge Mach numbers, but correspondingly high values of $Re_{\theta,E}/M_E$. The low edge Mach numbers for these experiments performed with sharp models suggested that the second-mode instability was not the dominant transition mechanism. This assumption was supported by the low N-factors calculated at the transition location. For these shots, an attempt was made to perform a stability analysis of oblique wave disturbances using STABL to capture the first mode. The results of the oblique wave analysis were inconclusive- we did not observe appreciable growth rates or N-factors suggesting oblique waves led to the transition of the boundary layer in these cases. Further analysis will be performed to validate our efforts.
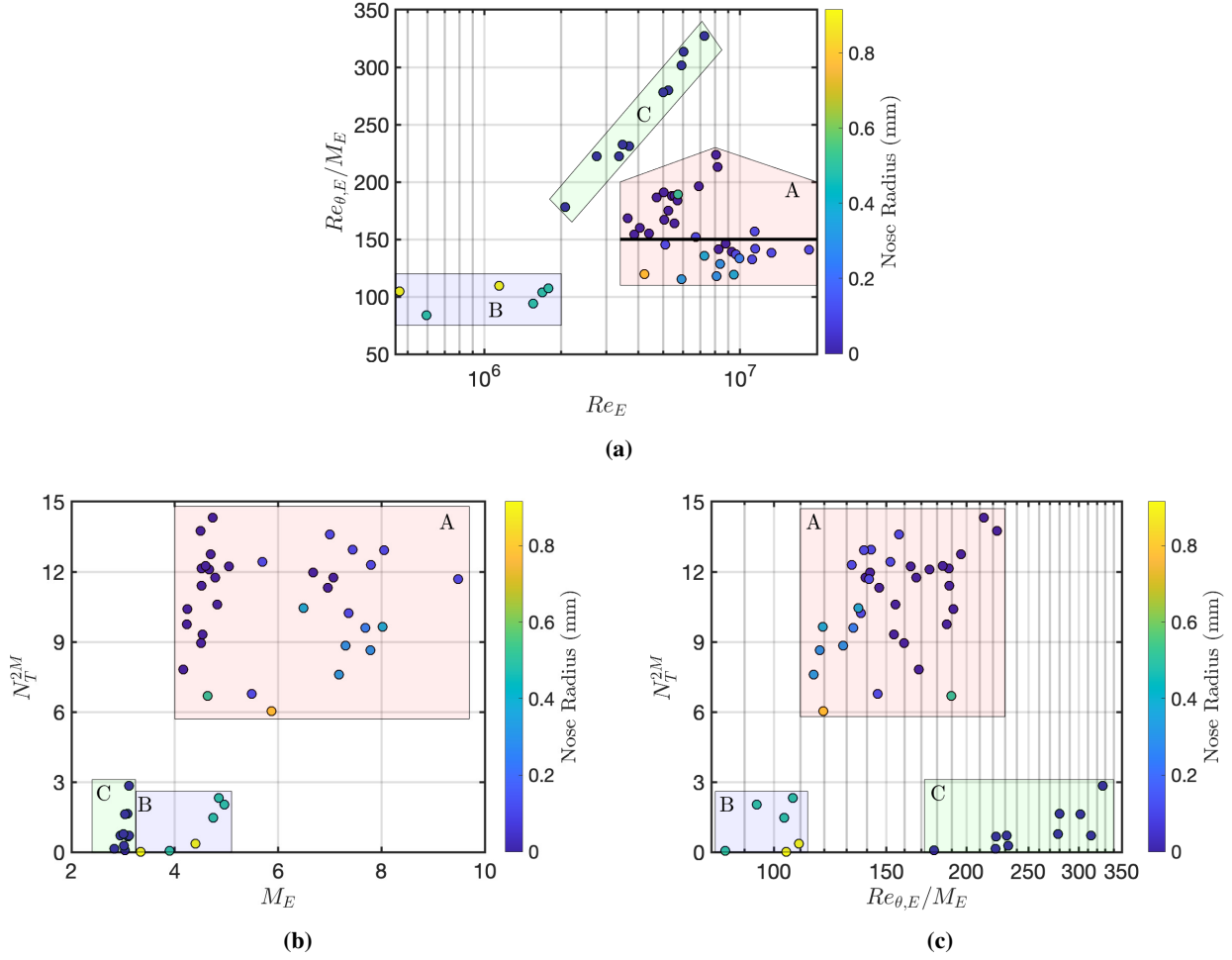
Fig. 8 **(a) The effect of the edge Reynolds number at the transition location on the transition parameter** $Re_{\theta,E}/M_E$ **computed at the transition location using edge conditions. (b) The maximum second mode N factor at the transition location as a function of the edge Mach number at the transition location (c) Comparing the maximum second mode N-factor at the transition location against the transition parameter,** $Re_{\theta,E}/M_E$, **distinctly divides the dataset into three groupings.**

To further investigate the effects of nose-tip bluntness on boundary-layer transition, we calculate the swallowing distance (S_{SW}), or the distance where the boundary-layer thickness becomes larger than the thickness of the entropy layer. To do this, we compute the entropy change in reference to the freestream as

$$ds = c_p \log(T/T_\infty) - R \log(P/P_\infty), \tag{5}$$

where c_p and R are the mass-specific heat at constant pressure and the gas constant, respectively. We define the entropy-layer thickness as the wall-normal location where the mass-specific entropy increases above the post-normal-shock mass-specific entropy. In Fig. 9, we show the change in entropy as determined using Eq. 5. The dashed black line in the figure is an estimation of the entropy-layer thickness and the solid black line represents the estimated boundary-layer thickness. The intersection of these two lines provides the swallowing distance, marked by the red circle at approximately 25 mm in the figure.

Fig. 10 shows the effects induced by the nose radius of the blunt models by plotting the computed second-mode N-factor at the transition location against the ratio of the transition location and the entropy-layer swallowing distance (swallowing distance ratio, S_T/S_{SW}). This figure is similar to Fig. 10 in Ref. 41. In Fig. 10, the experiments featuring a sharp nose tip (noted with an arrow on the right) are located at infinity on the abscissa. The experiments performed with
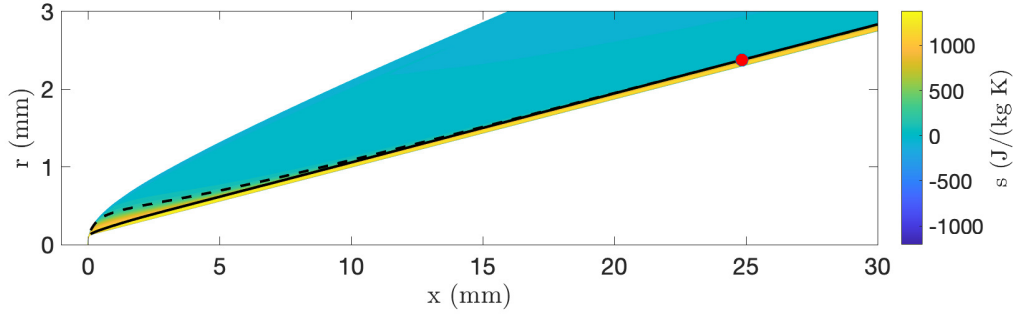
9

Fig. 9 Method of determining the entropy-layer swallowing distance. The entropy layer is computed as a change from the freestream. The result shown here is from shot 5699. The dashed line represents the entropy layer, and the solid line represents the boundary layer.

sharp models at low edge Mach numbers and low transition N-factors (group C in Fig. 8) are omitted from this plot. A trend similar to that presented by Jewell and Kimmel [41] is observed, however, the data presented here is shifted to the right by approximately an order of magnitude. We suspect this may be due to the experiment setup. The experiments performed by Sheetz, which are analyzed in this paper, were ballistic-range experiments featuring lower freestream noise, whereas the experiments analyzed by Jewell and Kimmel [41] were performed in a conventional wind tunnel. As the freestream noise in a conventional wind tunnel is higher, the initial disturbance amplitude is also higher. This indicates that transition would occur earlier at a lower N-factor.

For experiments where $S_T/S_{SW} < 1$, the second-mode N-factors are less than approximately 2, suggesting that an alternative to the second-mode instability may be the dominant transition mechanism for these shots. Possible alternatives proposed by Marineau et al. [42] include transient growth or the entropy-layer instability. At the start of the region where $S_T/S_{SW} > 1$, we note a short span where the transition N-factor increases from 6 to 11. This occurs before it appears to approach a limiting value of 13 for the experiments performed with models featuring a small nose-tip bluntness. As was previously discussed, there is a large spread observed in the N-factors for the experiments performed with sharp models.
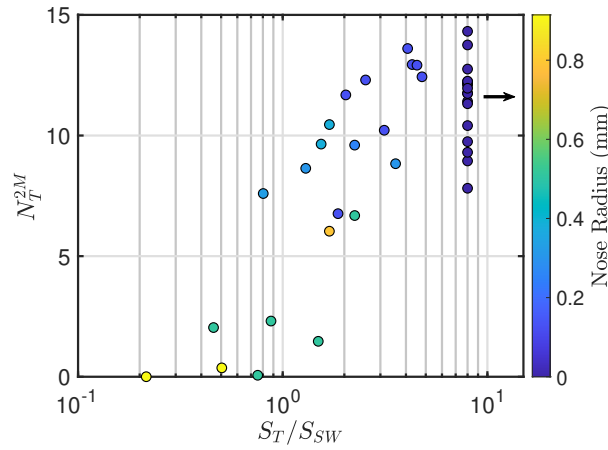
Fig. 10 Computed second mode N-factor at the transition location as a function of the swallowing distance ratio, S_T/S_{SW}. Experiments featuring a sharp nose tip (noted with an arrow on the right) are located at infinity on the abscissa, and those with low edge Mach numbers at the transition location (low second mode N-factor) are omitted.

In Fig. 11, we plot the edge Reynolds number at the transition location, R_E, with the N-factor for blunt and sharp cases on the left and only sharp cases on the right. There appears to be a statistically significant correlation between R_E at the transition location on the N-factor given that one ignores the cases with an $N_T^{2M} \approx 3$. For these cases, the analysis

Fig. 11   Dependency of the second mode N-factor at the transition location on the edge Reynolds number at the transition location for (a) all experiments performed by Sheetz and (b) only sharp experiments performed by Sheetz. Sensibly, at higher values of the edge Reynolds number generate higher maximum second mode N factors at the transition location.

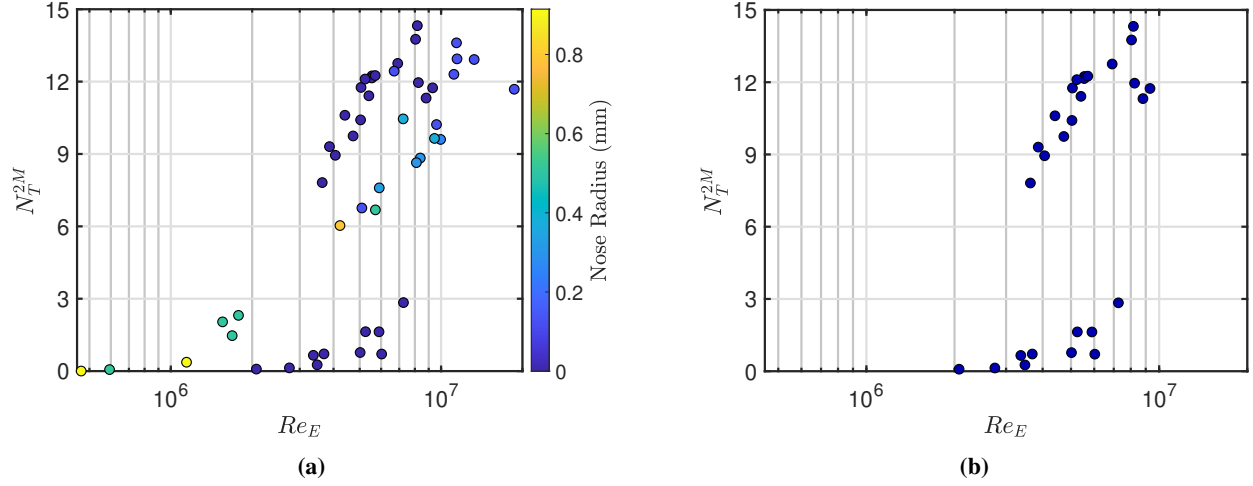is not dominated by the second-mode instability. Furthermore, if we eliminate the experiments which featured blunt models, as is done for Fig. 11b, this correlation appears more clear. It is sensible that higher values of the edge Reynolds number generate higher N_T^{2M}, suggesting this may be a means to assess uncertainty and repeatability.

D. Ongoing work: Shot 5776

To investigate the physical mechanisms leading to the early transition for shot 5776, we computed the disturbance flow-field using the time-spectral solver with a perfect gas assumption. The flow-field simulated after forcing slow acoustic waves in the free stream with a frequency of 6 and 7 MHz is shown in Figs. 12a and 12b, respectively, in terms of the real component of disturbance pressure. The boundary layer instabilities observed close to the wall are generated through the receptivity process at the nose. To identify the disturbances present in the flow-field, the phase speed is computed based on the wall pressure and plotted it in Fig. 12c. The phase speed of the slow ($c_r = 1 - 1/M_e$) and fast continuous acoustic ($c_r = 1 + 1/M_e$) waves are also shown in the figure in terms of dashed-dotted lines. As the edge Mach number varies along the cone, there is a significant variation in the phase speed of these two waves near the nose region. For all the frequency cases considered in the figure, the receptivity process at the nose leads to the generation of the fast mode with a velocity closer to the fast acoustic wave. Moving along the cone, the phase speed of the fast mode reduces slowly and it synchronizes with the entropy/vorticity branch ($c_r = 1$) around $x = 0.05$ m, indicated by the sharp oscillations. An upstream movement of this synchronization location is noticed with increasing frequency. Moving further downstream, the fast mode converts to Mack's second mode, which can be identified from the presence of two-cell structures near the wall in the disturbance flow-field. Downstream of $x = 0.155$ m, the phase speed value drops below $c_r = 1 - 1/M_e$, indicating the appearance of the supersonic mode in the flow at 6 MHz. The synchronization of the second mode with the slow acoustic waves leads to the emergence of the supersonic mode [43], which is recognized from the elongated structures in the disturbance flow-field. As the frequency is increased, the supersonic mode moves upstream of the cone (see Fig. 12b), and the onset of this mode in the flow-field is marked by a small square in the phase speed plot. Although at 6 and 7 MHz, the supersonic mode continues till the end of the cone, for the largest frequency case, the dominant mode downstream of $x = 0.16$ m is no longer this mode. However, there appears another mode whose phase speed oscillates around $c_r = 1$, indicating it travels with meanflow velocity.

A comparison of the wall pressure amplitude at three frequencies is presented in Fig. 12d when forced with SA waves. Initially, the disturbances seem to decay at the region where the first mode is the dominant instability. This is expected since the cases shown in the figure are computed using a zero azimuthal wavenumber, but the first mode attains a larger amplification at non-zero β. However, as the instability evolves to the second mode moving downstream, an exponential growth is observed which is largest for the 6 MHz case. As the frequency is increased, the dominant instability mode

11

(a) 6 MHz

(b) 7 MHz

(c) Phase speed

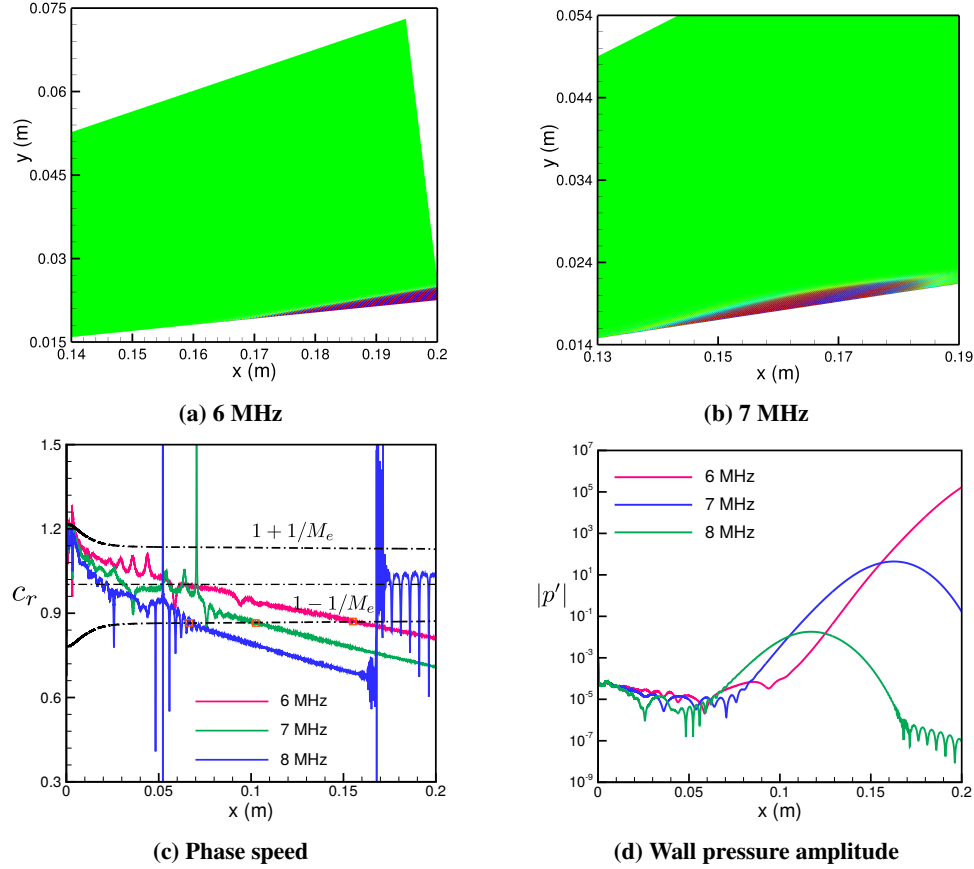**(d) Wall pressure amplitude**

Fig. 12   The disturbance pressure flow-field is shown in terms of the real component of pressure when forcing with SA waves at (a) 6 MHz and (b) 7 MHz. (c) Comparison of phase speed and (d) wall-pressure amplitude at three frequencies for shot 5776.

moves upstream with a reduction in the peak amplification rate. Although the experimental data suggests that transition occurs at $x = 0.025$ m, we do not observe any noticeable disturbance growth at this location. Since modal amplification is too weak to initiate transition at this location, non-modal growth can be a potential factor. To verify this, we computed the energy of the instability waves obtained after forcing three-dimensional disturbances. As the non-modal growth is associated with oblique traveling disturbances at low frequencies, we computed Mack's energy at 10 kHz and 100 kHz and plotted in Figs. 13a and 13b, respectively. In terms of disturbance amplitudes and mean flow, the integrated value of disturbance energy is calculated using Mack's norm as $E' = \frac{1}{2} \int_{\eta} (\bar{\rho}|u'|^2 + \bar{\rho}|v'|^2 + \bar{\rho}|w'|^2 + \bar{T}R|\rho'|^2/\bar{\rho} + \bar{\rho}C_v|T'|^2/\bar{T})d\eta$. The largest transient growth is observed for $\beta = 350$ at 10 kHz, which leads to an N-factor of 3.12 at the experimentally measured transition location, marked by the dashed-dotted line in Fig. 13. At 100 kHz, β ranging from 195 to 600 shows a similar N-factor of 3. The traveling waves with larger oblique inclination will rapidly reduce the transient energy growth as can be seen from Fig. 13b. Results indicate that non-modal amplification is also not enough to explain the early onset of transition as observed in the experiment. We note that while the present results are computed using a perfect gas assumption, the inclusion of real gas effects is expected to further stabilize the flow. In continuation of this work, we will look at the non-modal growth of traveling disturbances within the entropy layer for a range of oblique waves. In addition, we will also investigate the effect of forcing a combination of free-stream waves on the receptivity process and in turn how it influences the transition location.

VI. Conclusions

This paper analyzes hypervelocity ballistic-range transition experiments in STABL and CHAMPS. The stability calculations are nominally consistent and, in the cases where second mode should dominate transition, the N-factor of

(a) 10 kHz   **(b) 100 kHz**
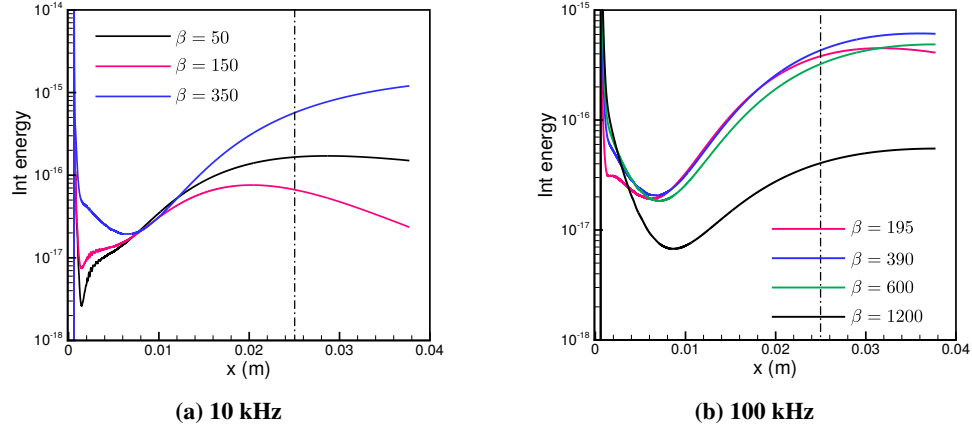
Fig. 13   Variation of integrated Mack's energy norm along the cone's surface for shot 5776 at different azimuthal wavenumber. The dashed-dotted line indicates the transition location observed in the experiment.

transition was found to be higher than that in conventional hypersonic facilities. We assess the spread of N-factor of transition for a subset of experiments where the geometry and physics governing transition should be the same (all sharp, 5° half-angle cones with high edge Mach number). The N-factor spread in these cases was found to be 7.8-14.3. Conventional transition location correlations are presented and, although they are not mechanism based, the correlations do appear to separate the data into distinct groupings which can inform further mechanism-based analysis.

Acknowledgments

13

Table 1 Conditions for the Sheetz experiments. Shot, θ_C, R_N, S_T, and S_{SW} are the shot number, nose radius, transition location along the model surface, and location along the model surface where the entropy layer is swallowed by the boundary layer. M, U, P, T, ρ, and Re^{Unit}, are the velocity, pressure, temperature, density, and unit Reynolds number, respectrively, with ∞ and E marking the freestream and edge conditions, respectively. N_T^{2M} is the N-factor of transition assuming second mode dominates.

Shot	θ_C	R_N	S_T	S_{SW}	M_∞	U_∞	P_∞	T_∞	ρ_∞	Re_∞^{Unit}	M_E	U_E	P_E	T_E	ρ_E	Re_E^{Unit}	N_T^{2M}
	(deg)	(µm)	(m)	(m)	(-)	(km/s)	(kPa)	(K)	(kg/m^3)	(1/m)	(-)	(km/s)	(kPa)	(K)	(kg/m^3)	(1/m)	(-)
4046	5.0	0	0.077	0.000	3.24	1.39	100.9	456	0.768	4.08e+07	3.10	1.37	121.3	484	0.869	4.36e+07	0.7
4047	5.0	0	0.089	0.000	3.26	1.32	83.4	409	0.708	3.87e+07	3.11	1.30	100.4	435	0.801	4.12e+07	0.7
4048	5.0	0	0.135	0.000	3.23	1.35	84.3	430	0.680	3.65e+07	3.09	1.32	101.3	457	0.769	3.89e+07	1.6
4050	5.0	0	0.174	0.000	3.26	1.31	81.4	397	0.711	3.91e+07	3.11	1.28	98.0	422	0.805	4.17e+07	2.8
4051	5.0	0	0.051	0.000	3.17	1.34	93.0	445	0.725	3.79e+07	3.03	1.32	111.2	472	0.818	4.04e+07	0.1
4056	5.0	0	0.136	0.000	3.17	1.35	101.0	450	0.779	4.06e+07	3.03	1.33	120.8	477	0.879	4.33e+07	1.6
4057	5.0	0	0.136	0.000	3.08	1.29	102.0	433	0.818	4.18e+07	2.95	1.27	121.1	458	0.918	4.43e+07	0.7
4058	5.0	0	0.108	0.000	3.15	1.30	101.7	423	0.834	4.37e+07	3.01	1.28	121.4	449	0.938	4.65e+07	0.8
4059	5.0	0	0.081	0.000	3.16	1.35	101.0	451	0.778	4.04e+07	3.02	1.33	120.7	478	0.877	4.31e+07	0.3
4060	5.0	0	0.074	0.000	2.95	1.32	105.7	498	0.736	3.50e+07	2.83	1.30	124.3	524	0.823	3.73e+07	0.1
5036	5.0	0	0.079	0.000	4.53	1.95	102.2	461	0.770	5.71e+07	4.24	1.93	137.6	511	0.934	6.36e+07	10.4
5037	5.0	0	0.075	0.000	4.52	1.94	100.2	455	0.764	5.67e+07	4.23	1.91	134.8	505	0.926	6.31e+07	9.7
5039	5.0	0	0.112	0.000	5.15	1.78	60.9	297	0.711	6.63e+07	4.73	1.76	86.9	342	0.882	7.29e+07	14.3
5040	5.0	0	0.102	0.000	5.11	1.77	57.4	298	0.669	6.19e+07	4.69	1.75	81.6	342	0.826	6.78e+07	12.8
5041	5.0	0	0.075	0.000	4.85	2.01	98.6	428	0.800	6.45e+07	4.51	1.99	136.8	481	0.987	7.24e+07	11.4
5042	5.0	0	0.057	0.000	4.85	2.04	99.2	437	0.787	6.32e+07	4.51	2.01	137.5	492	0.970	7.08e+07	8.9
5043	5.0	0	0.089	0.000	4.86	1.68	80.3	297	0.937	8.25e+07	4.49	1.66	111.4	338	1.145	9.02e+07	13.8
5049	5.0	0	0.068	0.000	5.50	2.54	124.7	531	0.816	7.16e+07	5.05	2.51	184.0	612	1.043	8.21e+07	12.2
5050	5.0	0	0.054	0.000	5.17	2.46	163.8	563	1.010	8.25e+07	4.78	2.43	234.1	640	1.269	9.40e+07	11.8
5051	5.0	0	0.073	0.000	4.85	2.15	120.3	489	0.854	6.71e+07	4.52	2.13	166.8	548	1.056	7.57e+07	12.2
5462	5.0	0	0.060	0.000	7.66	2.65	67.3	297	0.786	1.09e+08	6.96	2.63	123.0	354	1.206	1.46e+08	11.3
5467	5.0	0	0.049	0.000	4.89	2.28	140.7	539	0.906	7.05e+07	4.54	2.25	195.8	608	1.118	7.92e+07	9.3
5468	5.0	0	0.065	0.000	5.03	2.49	158.3	606	0.907	7.13e+07	4.66	2.45	223.2	686	1.130	8.08e+07	12.1
5469	5.0	0	0.052	0.000	4.44	1.95	119.5	478	0.868	6.27e+07	4.16	1.92	159.5	528	1.048	6.97e+07	7.8
5470	5.0	0	0.073	0.000	4.96	2.19	119.9	483	0.861	6.93e+07	4.60	2.16	168.0	546	1.067	7.79e+07	12.3
5474	5.0	0	0.064	0.000	8.29	2.87	72.0	296	0.844	1.27e+08	7.07	2.83	140.7	397	1.229	1.47e+08	11.7
5475	5.0	0	0.064	0.000	7.63	2.93	86.7	367	0.821	1.08e+08	6.68	2.90	158.4	467	1.176	1.28e+08	12.0
5499	5.0	0	0.050	0.000	5.20	2.65	175.7	644	0.946	7.61e+07	4.82	2.62	251.9	731	1.196	8.76e+07	10.6
5697	5.0	127	0.084	0.017	6.70	2.33	57.3	300	0.663	8.03e+07	5.70	2.28	95.3	398	0.832	8.00e+07	12.4
5699	5.0	127	0.102	0.025	8.30	2.89	57.5	300	0.666	9.98e+07	7.00	2.85	112.5	410	0.952	1.12e+08	13.6
5707	5.0	127	0.102	0.033	8.70	3.03	44.2	300	0.511	8.03e+07	7.36	2.99	90.0	409	0.764	9.43e+07	10.2
5708	6.3	305	0.071	0.020	11.10	3.86	57.9	300	0.670	1.34e+08	7.30	3.76	198.2	658	1.046	1.18e+08	8.8
5776	6.3	508	0.025	0.034	10.30	3.58	67.2	300	0.777	1.45e+08	3.90	3.07	187.1	1532	0.422	2.34e+07	0.1
5779	6.3	254	0.058	0.026	12.80	4.45	80.6	300	0.932	2.16e+08	7.69	4.33	334.4	787	1.473	1.71e+08	9.6
5802	6.3	127	0.079	0.018	9.90	3.44	60.2	300	0.697	1.25e+08	7.45	3.38	178.5	509	1.216	1.46e+08	12.9
5836	9.0	508	0.036	0.024	10.20	3.55	46.8	300	0.542	9.99e+07	4.74	3.27	234.0	1174	0.691	4.74e+07	1.5
5840	6.3	508	0.048	0.105	10.40	3.62	46.8	300	0.542	1.02e+08	4.96	3.34	145.1	1125	0.447	3.22e+07	2.0
5843	6.3	127	0.084	0.045	8.30	2.89	53.4	300	0.618	9.26e+07	5.49	2.76	129.4	629	0.714	6.08e+07	6.8
5857	6.3	127	0.079	0.031	10.70	3.96	63.2	339	0.647	1.21e+08	7.79	3.88	206.1	613	1.167	1.42e+08	12.3
5874	6.3	914	0.023	0.106	10.40	3.85	104.7	339	1.072	1.95e+08	3.34	3.04	254.4	1999	0.432	2.04e+07	0.0
5881	6.3	508	0.076	0.034	6.90	2.40	87.0	300	1.006	1.25e+08	4.64	2.27	176.1	592	1.032	7.50e+07	6.7
5885	6.3	127	0.089	0.020	11.10	3.86	53.9	300	0.624	1.25e+08	8.05	3.79	184.5	548	1.167	1.49e+08	12.9
5895	3.0	508	0.076	0.087	10.20	3.55	69.6	300	0.805	1.48e+08	4.85	3.25	105.6	1105	0.331	2.34e+07	2.3
1	6.3	381	0.107	0.063	9.00	3.13	38.8	300	0.449	7.30e+07	6.49	3.04	103.0	545	0.656	6.77e+07	10.5
2	6.3	381	0.107	0.069	13.30	4.63	37.5	300	0.433	1.04e+08	8.02	4.51	164.5	781	0.730	8.84e+07	9.6
3	6.3	127	0.066	0.032	15.00	5.22	77.6	300	0.898	2.43e+08	9.49	5.12	407.4	723	1.956	2.83e+08	11.7
4	6.3	305	0.066	0.051	15.00	5.22	61.6	300	0.712	1.93e+08	7.79	5.05	323.4	1039	1.078	1.23e+08	8.6
6	6.3	914	0.061	0.121	15.00	5.22	46.8	300	0.542	1.47e+08	4.40	4.53	226.9	2519	0.303	1.87e+07	0.4
7	9.0	787	0.097	0.057	10.00	3.48	23.4	300	0.271	4.90e+07	5.87	3.32	113.5	794	0.496	4.38e+07	6.0
8	9.0	330	0.041	0.051	15.00	5.22	52.2	300	0.604	1.64e+08	7.17	5.01	489.2	1206	1.405	1.45e+08	7.6

References

[1] Morkovin, M. V., "Critical Evaluation of Transition From Laminar to Turbulent Shear Layers with Emphasis on Hypersonically Traveling Bodies," AFFDL TR-68-149, 1969.

[2] Reshotko, E., "Boundary-Layer Stability and Transition," *Annual Review of Fluid Mechanics*, Vol. 8, 1976, pp. 311–349. https://doi.org/{10.1146/annurev.fl.08.010176.001523}.

[3] Saric, W. S., Reed, H. L., and Kerschen, E. J., "Boundary Layer Receptivity to Freestream Disturbances," *Annual Review of Fluid Mechanics*, Vol. 34, 2002, pp. 291–319. https://doi.org/{10.1146/annurev.fluid.34.082701.161921}.

[4] Fedorov, A., "Receptivity of a High-Speed Boundary Layer to Acoustic Disturbances," *Journal of Fluid Mechanics*, Vol. 491, 2003, pp. 101–129. https://doi.org/{10.1017/S0022112003005263}.

[5] Fedorov, A., "Transition and Stability of High-Speed Boundary Layers," *Annual Review of Fluid Mechanics*, Vol. 43, 2011, pp. 79–95. https://doi.org/10.1146/annurev-fluid-122109-160750.

[6] Schneider, S. P., "Effects of High-Speed Tunnel Noise on Laminar-Turbulent Transition," *Journal of Spacecraft and Rockets*, Vol. 38, No. 3, 2001, pp. 323–333. https://doi.org/10.2514/2.3705.

[7] Schneider, S. P., "Hypersonic Laminar-Turbulent Transition on Circular Cones and Scramjet Forebodies," *Progress in Aerospace Sciences*, Vol. 40, No. 1-2, 2004, pp. 1–50. https://doi.org/10.1016/j.paerosci.2003.11.001.

[8] Bushnell, D., "Notes on Initial Disturbance Fields for the Transition Problem," *Instability and Transition*, edited by M. Hussaini and R. Voigt, ICASE/NASA LaRC Series, Springer US, 1990, pp. 217–232. https://doi.org/10.1007/978-1-4612-3430-2_28.

[9] Laufer, J., "Some Statistical Properties of the Pressure Field Radiated by a Turbulent Boundary Layer," *Physics of Fluids (1958-1988)*, Vol. 7, No. 8, 1964, pp. 1191–1197. https://doi.org/10.1063/1.1711360.

[10] Blanchard, A., Lachowicz, J., and Wilkinson, S., "Performance of the NASA-Langley Mach 6 Quiet Wind Tunnel," *AIAA Journal*, Vol. 35, No. 1, 1996, pp. 23–28. https://doi.org/10.2514/6.1996-441.

[11] Schneider, S. P., "Development of Hypersonic Quiet Tunnels," *Journal of Spacecraft and Rockets*, Vol. 45, No. 4, 2008, pp. 641–664. https://doi.org/10.2514/1.34489.

[12] Hofferth, J. W., Humble, R. A., Floryan, D. C., and Saric, W. S., "High-Bandwidth Optical Measurements of the Second-Mode Instability in a Mach 6 Quiet Tunnel," *Proceedings of 51st AIAA Aerospace Sciences Meeting Including the New Horizons Forum and Aerospace Exposition*, AIAA 2013-0378, Grapevine, Texas, 2013. https://doi.org/10.2514/6.2013-378.

[13] Lyons, W. C., and Sheetz, N. W., "Transition Measurements on Cones in Free-Flight Ballistics-Range Tests," *Journal of the Aerospace Sciences*, Vol. 29, No. 3, 1962, pp. 352–352. https://doi.org/10.2514/8.9424.

[14] Lyons, W. C., and Sheetz, N. W., "Free Flight Experimental Investigations of the Effect of Boundary Layer Cooling on Transition," NOLTR 61-82, AD271681, 1962.

[15] Sheetz, N. W., "Free-Flight Boundary Layer Transition Investigations at Hypersonic Speeds," *Proceedings of the 2nd Aerospace Sciences Meeting*, AIAA-1965-0127, New York, New York, 1965. https://doi.org/10.2514/6.1965-127.

[16] Sheetz, N. W., "Ballistics Range Boundary-Layer Transition Measurements on Cones at Hypersonic Speeds," *Proceedings of the Symposium on Viscous Drag Reduction held at the LTV Research Center*, Dallas, Texas, September 24-25, 1968, pp. 53–83. https://doi.org/10.1007/978-1-4899-5579-1_3.

[17] Sheetz, N. W., "Ballistics Range Experiments on the Effect of Unit Reynolds Number on Boundary-Layer Transition," *8th Navy Symposium on Aeroballistics*, AD857473, Corona, California, May 6-8, 1969, pp. 201–214.

[18] Potter, J. L., "Observations on the Influence of Ambient Pressure on Boundary-Layer Transition," AEDC TR68-63, 1968.

[19] Potter, J. L., "Studies of Boundary-Layer Transition on Aeroballistic Range Models," AEDC TR-73-194, 1973.

[20] Potter, J. L., "Boundary-Layer Transition on Supersonic Cones in an Aeroballistic Range," *Proceedings of 12th Aerospace Sciences Meeting*, AIAA-1974-0132, Washington, D.C., 1974. https://doi.org/10.2514/6.1974-132.

[21] Potter, J. L., "Boundary-Layer Transition on Supersonic Cones in an Aeroballistic Range," *AIAA Journal*, Vol. 13, No. 3, 1975, pp. 270–277. https://doi.org/10.2514/3.49692.

[22] Reda, D. C., "Boundary-Layer Transition Experiments on Sharp, Slender Cones in Supersonic Freeflight," ADA054591 or NSWC/WOL TR-77-59, 1977.

[23] Reda, D. C., "Boundary-Layer Transition Experiments on Sharp, Slender Cones in Supersonic Freeflight," *Proceedings of 11th Fluid and Plasma Dynamics Conference*, AIAA-1978-1129, Seattle, Washington, 1978. https://doi.org/10.2514/6.1978-1129.

[24] Reda, D. C., "Boundary-Layer Transition Experiments on Sharp, Slender Cones in Supersonic Free Flight," *AIAA Journal*, Vol. 17, No. 8, 1979, pp. 803–810. https://doi.org/10.2514/3.61231.

[25] Swanson, T., and Daniel, D., "Hypersonic Boundary Layer Transition Experiments in Hypervelocity Ballistic Range G," *Proceedings of 54th AIAA Aerospace Sciences Meeting*, AIAA 2016-2118, San Diego, California, 2016. https://doi.org/10.2514/6.2016-2118.

[26] Mueschke, N. J., Walker, J. D., and Grosch, D., "Examination of Atmospheric Density Scaling Effects on Sub-Scale Hypersonic Flight Bodies Using a Ballistic Launch Facility," *Proceedings of the 23rd AIAA International Space Planes and Hypersonic Systems and Technologies Conference*, AIAA-2020-2444, Montreal, Quebec, Canada, 2020. https://doi.org/10.2514/6.2020-2444.

[27] Johnson, H. B., Seipp, T. G., and Candler, G. V., "Numerical Study of Hypersonic Reacting Boundary Layer Transition on Cones," *Physics of Fluids*, Vol. 10, No. 13, 1998, pp. 2676–2685. https://doi.org/10.1063/1.869781.

[28] Johnson, H. B., "Thermochemical Interactions in Hypersonic Boundary Layer Stabity," Ph.D. thesis, University of Minnesota, Minneapolis , Minnesota, 2000.

[29] Wright, M. J., Candler, G. V., and Prampolini, M., "Data-parallel Lower-upper Relaxation Method for the Navier-Stokes Equations," *AIAA Journal*, Vol. 34, No. 7, 1996, pp. 1371–1377. https://doi.org/10.2514/3.13242.

[30] Johnson, H., and Candler, G., "Analysis of laminar-turbulent transition in hypersonic flight using PSE-Chem," *36th AIAA Fluid Dynamics Conference and Exhibit*, AIAA-2006-3057, San Francisco, California, 2006. https://doi.org/10.2514/6.2006-3057.

[31] Araya, D., Bitter, N., Wheaton, B. M., Kamal, O., Colonius, T., Knutson, A., Johnson, H., Nichols, J., Candler, G. V., Russo, V., and Brehm, C., "Assessment of Linear Methods for Analysis of Boundary Layer Instabilities on a Finned Cone at Mach 6," *AIAA AVIATION 2022 Forum*, AIAA-22-03247, Chicago, IL, 2022. https://doi.org/10.2514/6.2022-3247, URL https://arc.aiaa.org/doi/abs/10.2514/6.2022-3247.

[32] Browne, O. M. F., Haas, A. P., Fasel, H. F., and Brehm, C., "An efficient linear wavepacket tracking method for hypersonic boundary-layer stability prediction," *J. Comput. Phys.*, Vol. 380, 2019, pp. 243–268.

[33] Browne, O. M., Haas, A. P., Fasel, H. F., and Brehm, C., "A nonlinear compressible flow disturbance formulation for adaptive mesh refinement wavepacket tracking in hypersonic boundary-layer flows," *Computers Fluids*, Vol. 240, 2022, p. 105395. https://doi.org/https://doi.org/10.1016/j.compfluid.2022.105395, URL https://www.sciencedirect.com/science/article/pii/S0045793022000652.

[34] Haas, A. P., Browne, O. M., Fasel, H. F., and Brehm, C., "A Numerical Jacobian Based Linearized Compressible Navier-Stokes Solver For Hypersonic Boundary-Layer Stability," *47th AIAA Fluid Dynamics Conference*, 2017, p. 4520.

[35] Haas, A. P., Browne, O. M., Fasel, H. F., and Brehm, C., "A time-spectral approximate Jacobian based linearized compressible Navier-Stokes solver for high-speed boundary-layer receptivity and stability," *Journal of Computational Physics*, Vol. 405, 2020, p. 108978.

[36] Balay, S., Gropp, W. D., McInnes, L. C., and Smith, B. F., "Efficient management of parallelism in object-oriented numerical software libraries," *Modern software tools for scientific computing*, Springer, 1997, pp. 163–202.

[37] Amestoy, P. R., Duff, I. S., and L'Excellent, J.-Y., "MUMPS multifrontal massively parallel solver version 2.0," 1998.

[38] Balakumar, P., "Receptivity of supersonic boundary layers to acoustic disturbances over blunt cones," *37th AIAA Fluid Dynamics Conference and Exhibit*, 2007, p. 4491.

[39] Kara, K., Balakumar, P., and Kandil, O., "Receptivity of hypersonic boundary layers due to acoustic disturbances over blunt cone," *45th AIAA Aerospace Sciences Meeting and Exhibit*, 2007, p. 945.

[40] Balakumar, P., "Receptivity of hypersonic boundary layers to acoustic and vortical disturbances," *45th AIAA Fluid Dynamics Conference*, 2015, p. 2473.

[41] Jewell, J. S., and Kimmel, R. L., "Boundary-layer stability analysis for Stetson's Mach 6 Blunt-cone experiments," *Journal of Spacecraft and Rockets*, Vol. 54, No. 1, 2017, pp. 258–265. https://doi.org/10.2514/1.A33619.

[42] Marineau, E. C., Moraru, G. C., Lewis, D. R., Norris, J. D., Lafferty, J. F., Wagnild, R. M., and Smith, J. A., "Mach 10 boundary layer transition experiments on sharp and blunted cones," *19th AIAA International Space Planes and Hypersonic Systems and Technologies Conference*, AIAA-2014-3108, Atlanta, Georgia, 2014. https://doi.org/10.2514/6.2014-3108.

[43] Saikia, B., Al Hasnine, S., and Brehm, C., "On the role of discrete and continuous modes in a cooled high-speed boundary layer flow," *Journal of Fluid Mechanics*, Vol. 942, 2022, p. R7.